J Mater Sci (2026) 61:11013–11024

Composites & nanocomposites

Microporous ZIF-8 nanocoating as a sensitive interface for SPR detection of antimony (III)

Muhammad Fahmi Anuar[1], Yap Wing Fen[1,2,*], Josephine Liew Ying Chyi[1,2], Huda Abdullah[3], Ahmad Taufiq[4], Nurul Hidayat[4], Tan Sin Tee[2], and Mohd Adzir Mahdi[1,5]

[1] *Functional Nanotechnology Devices Laboratory (FNDL), Institute of Nanoscience and Nanotechnology, (ION2) UPM 43400 Serdang Selangor, Malaysia*
[2] *Department of Physics, Faculty of Science, Universiti Putra Malaysia, 43400 UPM Serdang, Selangor, Malaysia*
[3] *Department of Electrical, Electronic, and Systems Engineering, Faculty of Engineering and Built Environment, Universiti Kebangsaan Malaysia UKM, 43600 Bangi, Selangor, Malaysia*
[4] *Department of Physics, Faculty of Mathematics and Natural Science, Universitas Negeri Malang, Jl. Semarang, Malang 65145, Indonesia*
[5] *Wireless and Photonics Networks, Faculty of Engineering, Universiti Putra Malaysia, 43400 UPM Serdang, Selangor, Malaysia*

Received: 22 December 2025
Accepted: 22 February 2026
Published online: 14 March 2026

ABSTRACT

ZIF-8 was successfully synthesised with a rhombic dodecahedral morphology, an average particle size of 262.60 ± 44.21 nm, a predominantly microporous framework, and a high surface area of 991.81 m^2/g. These structural features provide abundant adsorption sites, making ZIF-8 a suitable candidate for metal ion sensing. Integrated onto a gold SPR platform, the Au/ZIF-8 sensing layer exhibited clear resonance angle shifts toward higher angles in response to increasing $Sb3^+$ concentrations. The sensor achieved a strong linear response (R2 = 0.95), a sensitivity of 0.057°ppm^{-1}, and a binding affinity constant of 1.202 ppm^{-1}, demonstrating efficient interaction between ZIF-8 and Sb^{3+} ions. Overall, the physical, chemical, and optical properties of ZIF-8, together with its good reproducibility, make it a strong candidate for SPR-based antimony detection.

Introduction

Porous crystalline materials such as zeolitic imidazolate frameworks (ZIFs), particularly ZIF-8, have gained significant attention in recent years for their promising role in chemical sensing. Their popularity was due to their distinctive structural properties such as large surface area, tunable pore size, and exceptional chemical and thermal stability [1, 2]. Aside from that, ZIF-8 consists of a specific pore size to accommodate certain species including nanomaterials, receptors and even biomolecules [3]. Benefiting from these properties, ZIF-8 has been widely studied as a material in variety of potential applications such as gas storage [4, 5], separation [6, 7], catalysis [8–11], drug delivery [12–14], and sensing [15, 16].

Handling Editor: Oleksandr Savatieiev.

Address correspondence to E-mail: yapwingfen@upm.edu.my

https://doi.org/10.1007/s10853-026-12482-9

Although numerous ZIF-8-based sensors have been developed, most reported studies rely heavily on electrochemical sensors [17–20], where ZIF-8 serves as a catalytic or adsorptive layer to improve charge-transfer processes. However, its potential in optical sensing, particularly surface plasmon resonance (SPR), remains largely underexplored. In the context of plasmonic sensing, the intrinsic characteristics of ZIF-8 closely align with the optical requirements of SPR sensors. Its high surface area and tunable porosity facilitate the efficient adsorption and pre-concentration of target analyte near the gold interface, thereby enhance the local refractive index changes that enable the SPR signal to respond more effectively. Therefore, employing ZIF-8 in an SPR configuration could unlock new advantages, including enhanced analyte-sensor interactions, improved sensitivity, and more efficient detection of metal ions such as antimony (Sb^{3+}).

In particular, the detection of antimony has become increasingly important due to its rising presence in industrial effluents, electronic waste, mining discharges, and contaminated water sources [21]. This concern stems from the fact that antimony, especially in its trivalent form (Sb^{3+}), is highly toxic, persistent, and capable of bioaccumulating in aquatic and environmental ecosystems [22]. It is well established that excessive exposure to antimony can cause adverse health effects in both humans and animals, affecting several organs, including the lungs, heart, liver, and kidneys, and may also lead to gastrointestinal disorders [23–25]. Therefore, the ability to accurately and sensitively detect antimony ions is crucial for effective environmental monitoring, risk assessment, and the prevention of long-term ecological and public health impacts. As industrialisation continues to grow, the need for rapid, reliable, and low-cost sensing platforms becomes increasingly important to protect the environment and safeguard human health from long-term antimony exposure [26].

Given the limited attention toward integrating ZIF-8 with optical detection systems, there is a clear need to explore its potential within SPR-based sensing. Unlike the many ZIF-8 sensors that rely on electrochemical approaches, SPR provides label-free, real-time detection with high refractive-index sensitivity [27–29]. Therefore, this study is motivated to synthesise and characterize ZIF-8, examine its structural and surface properties, and evaluate its suitability as an active layer for enhancing SPR detection of antimony (Sb^{3+}).

Materials and methodologies

Materials

Zinc nitrate hexahydrate ($Zn(NO_3)_2.6H_2O$), 2-methylimidazole (HMIM), and methanol were purchased from Sigma-Aldrich (USA). The solution of 1000 ppm antimony (Sb) ions was purchased from Fisher Scientific (United Kingdom), and deionised water.

Preparation of target ions

Sb^{3+} stock solutions of 1000 ppm were diluted by using dilution formula $M_1V_1 = M_2V_2$ using deionised water to produce Sb^{3+} solutions with concentration of 0.01, 0.1, 1, 10, 100, and 1000 ppm. All solutions were prepared at room temperature.

Synthesis of ZIF-8

For the synthesis of ZIF-8, two solutions were prepared beforehand. First, Solution I was prepared by adding 2.975 g of $Zn(NO_3)_2.6H_20$ in 50 mL of methanol solution. Then, Solution II of 3.284 g of 2-methylimidazole in 50 mL of the same solvent was prepared. After that, the prepared Solution II, which contains the organic ligand, was carefully poured into Solution I under continuous magnetic stirring for 30 min. The mixture was then allowed to sit at room temperature for 24h. The centrifugation process was then performed on the mixture, and the resultant white solid was washed with methanol twice before being dried in an electrical oven overnight at 60 °C. The final product or the obtained white ZIF-8 powder was dispersed in fresh methanol for preparation of sensing films. Figure 1 illustrates the brief synthesis procedure of ZIF-8.

Integration of ZIF-8 with SPR

Preparation of the ZIF-8 thin film was first carried out before the incorporation with the SPR sensor. Prior to deposition, glass substrates (24 mm × 24 mm, thickness 0.13–0.16 mm) were thoroughly cleaned with acetone to remove surface impurities such as dust and fingerprints. Gold (Au) thin films were then deposited onto the glass using a sputter-coating technique. A K575X sputter coater (Quorum Technologies, West Sussex, UK) was employed, as

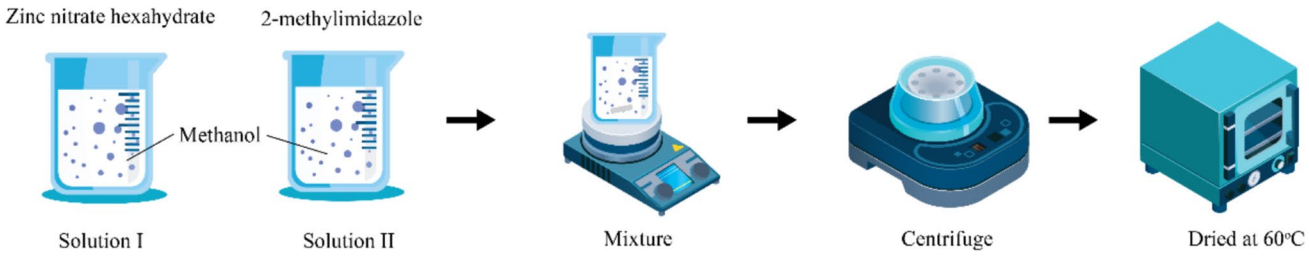

Figure 1 Synthesis method of zeolitic imidazolate framework-8 (ZIF-8).

it provides precise control over coating parameters and enables consistent gold film thickness across the substrate. To prepare the sensing layer, 1.0 mL of the ZIF-8 dispersed in methanol was deposited on top of the gold-coated thin film by using a spin coating machine (Specialty Coating System, P-6708D) to produce Au/ZIF-8 thin film for SPR sensor. The glass slip was spun at 6000 rpm for 30s to ensure uniform thickness. After coating, the samples were dried at 70 °C for 30 min to remove any remaining solvents and to improve the adhesion of the gold film on the glass substrate. The thin film was placed between the dielectric medium and the prism following the Kretschmann configuration [30] for the sensing measurements. Subsequently, Sb^{3+} solutions of varying concentrations, beginning from the lowest level up to 1000 ppm, were introduced onto the thin film, and the reflected light intensity at each angular interval was systematically recorded.

Results and discussion

Characterisation of synthesised ZIF-8 for SPR sensing layer

The morphological structure of the synthesised ZIF-8 was investigated by the FESEM image. Figure 2 showed the morphological surface of the ZIF-8 material before and after deposition onto gold thin film. From Fig. 1, clearly the particle powder was observed to be in the typical rhombic dodecahedron shape that was mentioned and agreed by several other researchers [31–34]. The synthesised ZIF-8 was initially observed to agglomerate into large clusters [9]. However, when comparing the two images, the ZIF-8 particles in Fig. 2b appear well distributed and less aggregated following the deposition process. This improvement can be attributed to the spin coating deposition method, which effectively spreads the ZIF-8 over the gold thin film, ensuring a high surface area-to-volume ratio and enhancing the sensor's overall performance.

Further measurements and analysis using ImageJ software showed that the average particle size of the synthesised ZIF-8 was 262.60 ± 44.21 nm. The particle size distribution, illustrated in Fig. 3, ranged from 150

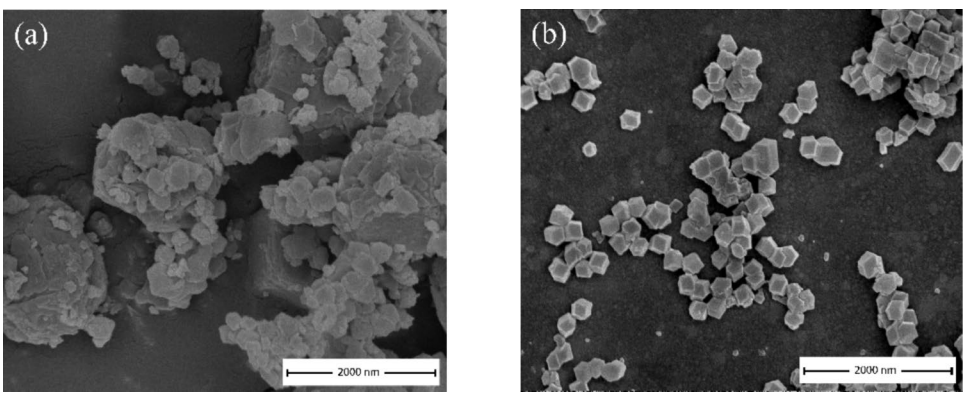

Figure 2 FESEM micrographs of ZIF-8 showing. **a** the morphology of synthesised powder and **b** the surface structure of the deposited thin film, each obtained at 50,000 × magnification.

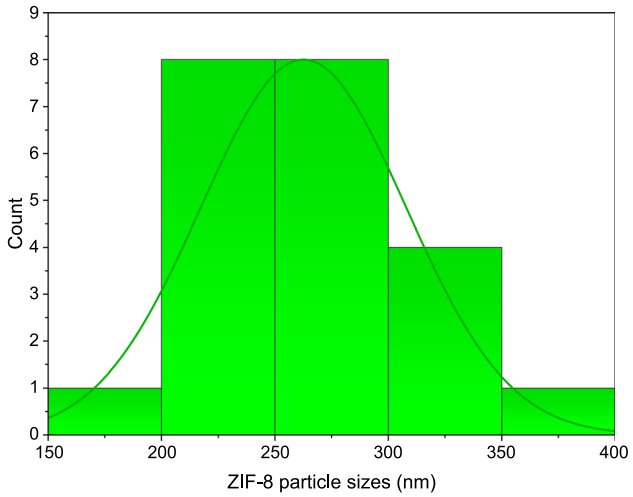

Figure 3 Particle sizes distribution of synthesised ZIF-8 range from 150–400 nm.

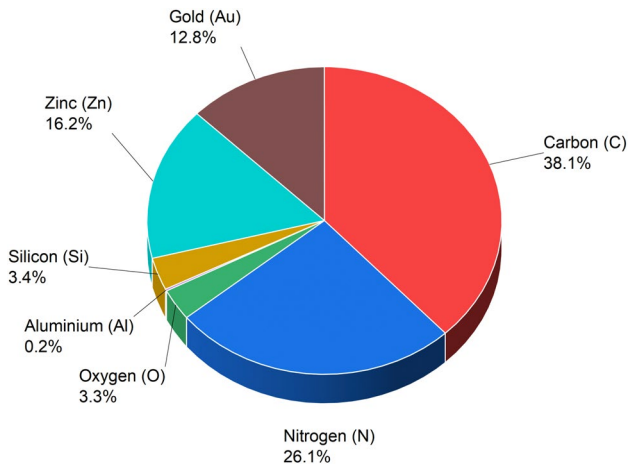

Figure 4 Elemental composition of synthesised ZIF-8 from EDX analysis.

Table 1 EDX quantitative analysis of ZIF-8 elemental compositions

Elements	Weight percentage (%)
Carbon (C)	38.08 ± 0.58
Nitrogen (N)	26.06 ± 0.97
Oxygen (O)	3.29 ± 1.51
Aluminium (Al)	0.21 ± 0.02
Silicon (Si)	3.41 ± 0.17
Zinc (Zn)	16.19 ± 0.58
Gold (Au)	12.76 ± 0.38

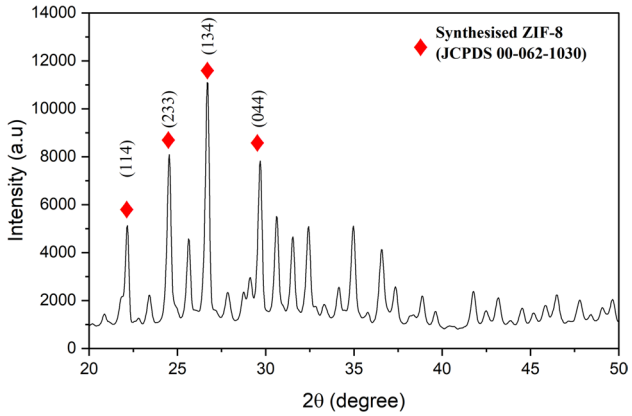

Figure 5 X-Ray diffraction (XRD) pattern of the synthesised ZIF-8 powder.

to 400 nm, which is in close agreement with previously reported values [35–37], thereby further confirming the consistency of the synthesis method. To complement the morphological study, Energy Dispersive X-Ray (EDX) spectroscopy analysis was carried out to determine quantitative values of the existing elements in the synthesised ZIF-8. Figure 4 and Table 1 present the elemental data obtained from the surface of the sensor, revealing the presence of carbon (C), nitrogen (N), zinc (Zn), and oxygen (O), which correspond to the expected elemental composition of ZIF-8 [38]. Additional elements detected are attributed to the glass substrate used as the underlying support for the sensing film. This data validates that the ZIF-8 was successfully synthesised and incorporated onto the sensing film's surface.

Aside from that, XRD analysis was also performed to further confirm the successful synthesis of ZIF-8. Figure 5 shows the XRD pattern of the synthesised sample with several distinct peaks at $2\theta = 22.1°$, 24.5°, 26.7° and 29.6°. These peaks are indicative of the material's highly ordered structure and are consistent with the data provided in the JCPDS 00–062–1030 card, as well as previously reported results [39], confirming the successful formation of zeolitic imidazolate framework-8 (ZIF-8).

The textural properties of the synthesised ZIF-8 were further investigated using nitrogen adsorption–desorption analysis, as shown in Fig. 6. The sample was classified as Type I according to the IUPAC classification, which is characteristic of materials with a predominantly microporous nature [40, 41]. The steep nitrogen uptake at relative pressure

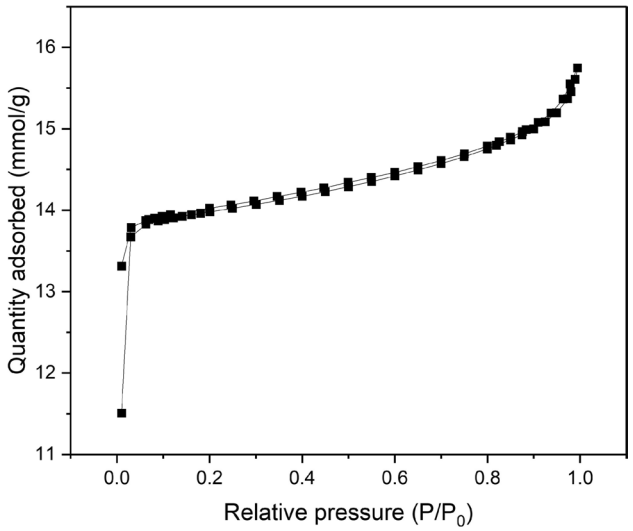

Figure 6 Nitrogen adsorption–desorption isotherm of the ZIF-8 sample synthesised.

($P/P_0 < 0.1$) corresponds to the filling of the samples micropores within the framework. In addition, the average pore diameter derived from BET analysis was 16.12 Å (adsorption) and 21.08 Å (desorption), consistent with the microporous classification. At higher relative pressures, a slight hysteresis loop was observed, indicating the presence of interparticle voids and larger mesopores formed between adjacent ZIF-8 crystallites [42]. The pore volume analysis further supported this finding, where the micropore volume was determined to be 0.3998 cm^3/g, with a total pore volume of 0.5227 cm^3/g, indicating a dominant microporous nature with minor mesoporous contributions. Furthermore, the BET surface area was calculated to be 991.81 m^2/g, while the micropore volume from BET analysis was 0.464 cm^3/g. The pore size distribution obtained using the Barrett–Joyner–Halenda (BJH) method (Fig. 7) shows a broad distribution in the range of 18–185 Å, indicating the coexistence of micropores and mesopores in the ZIF-8 structure [43]. According to the definition established by the International Union of Pure and Applied Chemistry (IUPAC), pores with diameters less than 2 nm are classified as micropores, those between 2 and 50 nm as mesopores, and those larger than 50 nm as macropores [44, 45]. Within this distribution, a sharp and intense peak at pore widths below approximately 20 Å is observed, confirming the predominantly microporous nature of the material. The high peak intensity further reflects a large volume of micropore within the structure where majority of the adsorption takes place.

SPR signal for Au/ZIF-8 towards Sb^{3+} ions

For potential antimony detection using the Au/ZIF-8 sensing layer, a preliminary SPR measurement was conducted by bringing the ZIF-8–modified gold thin film into contact with deionised water (DW) to establish a baseline response and determine the reference resonance angle. Figure 8 presents the SPR curve, where the incident angle is plotted on the x-axis and the reflectance intensity on the y-axis. The resonance

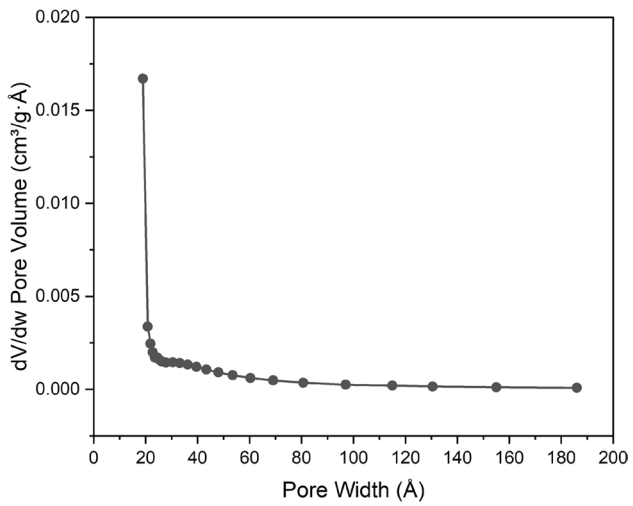

Figure 7 BJH pore size distribution curves of the synthesised ZIF-8.

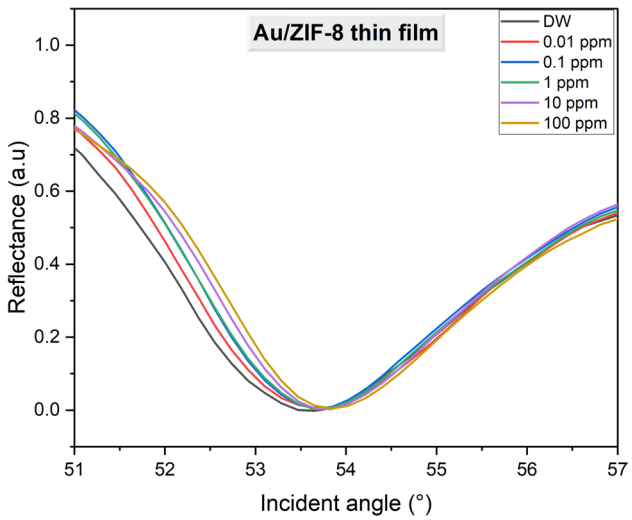

Figure 8 Experimental SPR curve of Au/ZIF-8 in contact with different concentrations of antimony ions from 0–100 ppm.

angle is identified by locating the minimum point of the reflectance dip, which corresponds to the excitation of surface plasmon. The baseline resonance angle was identified at 53.77°.

Upon introducing Sb^{3+}, the resonance angle shifted to 53.86°, corresponding to an incremental change of 0.097°. Overall, it was observed that the SPR curve was right-shifted with increasing concentrations of antimony ions. The observed shifts in resonance angle further verify the adsorption capability of the Au/ZIF-8 sensing layer toward antimony ions. These angular changes reflect variations in the local refractive index at the sensing interface, which occur as a result of increased adsorption or binding interactions between the ZIF-8-modified surface and the Sb^{3+} solution. This relationship confirms that the Au/ZIF-8 layer effectively responds to changes in analyte concentration, demonstrating its potential suitability for antimony detection using SPR. Each resonance angle shift corresponding to the respective Sb^{3+} concentrations was carefully recorded, and these measured values were subsequently utilised to calculate and evaluate the overall sensitivity of the Au/ZIF-8 SPR sensing platform as plotted in Fig. 9. From the graph, a good linear relationship between the Au/ZIF-8 and Sb^{3+} ions was observed, with the slope representing the sensor's sensitivity calculated at 0.057 ppm^{-1}. The linear regression yielded a strong coefficient of determination, R^2 of 0.95 within the concentration range of 0–100 ppm.

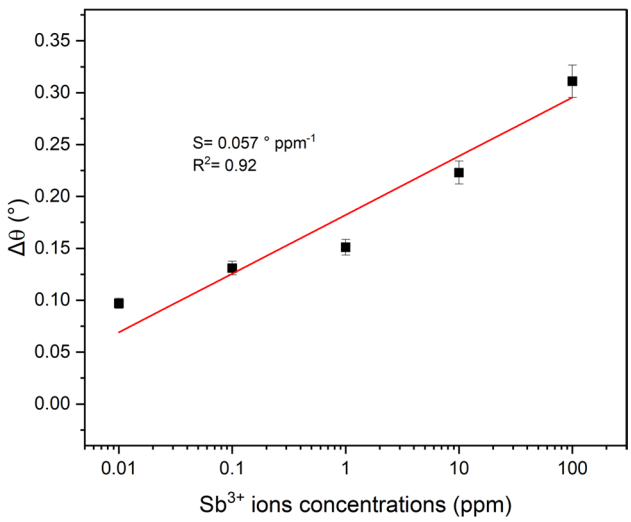

Figure 9 Sensitivity of Au/ZIF-8 sensor film for detection of Sb^{3+} of different concentrations (0–100 ppm).

While sensitivity reflects the response of the sensor to changes in analyte concentration, the practical applicability of the sensor is more comprehensively assessed through its limit of detection (LOD) using the equation below [46]:

$$LOD = \frac{3\sigma}{S} \tag{1}$$

where σ is the standard deviation obtained from blank measurement (number of replicates = 3). The σ value was determined to be 0.00112°. Accordingly, the limit of detection (LOD) for the Au/ZIF-8 thin-film-based SPR sensor toward Sb^{3+} detection was calculated to be 0.0589 ppm.

Complementing these observations, the binding affinity in this study was analysed using adsorption models such as Langmuir and Sips. The Langmuir isotherm model can be defined as:

$$\Delta\theta = \frac{\Delta\theta \max C}{C + \frac{1}{K}} \tag{2}$$

while the Sips isotherm model can be defined as:

$$\Delta\theta = \frac{\Delta\theta \max (KC)^n}{1 + (KC)^n} \tag{3}$$

where K is the binding affinity constant and n is the heterogeneity index of the system. The experimental data were fitted to the Sips isotherm model, and the goodness of fit was evaluated by comparing the coefficients of determination (R^2) from both the Langmuir and Sips models. The higher value indicates a better fit of the data with the corresponding model, thus providing insight into the nature and uniformity of the analyte and sensor layer interaction. The Langmuir model represents monolayer adsorption on homogeneous sites, whereas the Sips model incorporates surface heterogeneity, offering a more realistic depiction of the interaction between the sensing layer and the target analyte.

This non-linear fitting, as shown in Fig. 10 was used to study the interaction between the Au/ZIF-8 sensing layer and the Sb^{3+} ions. Based on the correlation of determination (R^2), the Sips model provided the best fit to the experimental data with R^2 of 0.82, indicating that the adsorption of Sb^{3+} on the Au/ZIF-8 surface is influenced by heterogeneous active sites rather than a uniform monolayer adsorption process [47]. The binding affinity constant, K was calculated to be 1.202 ppm^{-1} reflecting a good interaction Sb^{3+} ions and

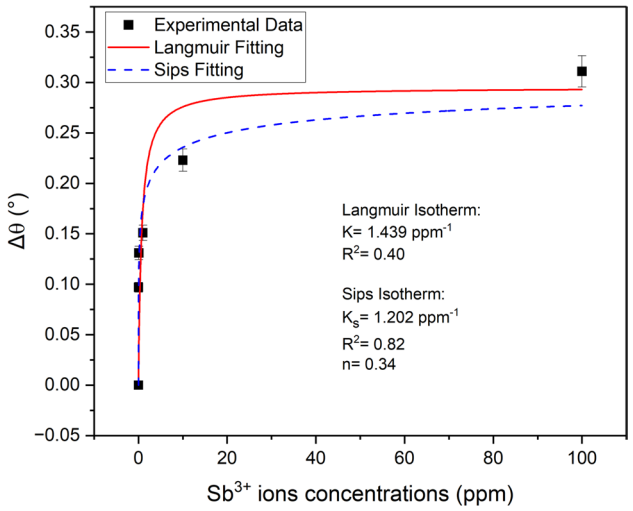

Figure 10 Experimental data fitted to Langmuir and Sips isotherm model for adsorption of Sb^{3+} on Au/ZIF-8.

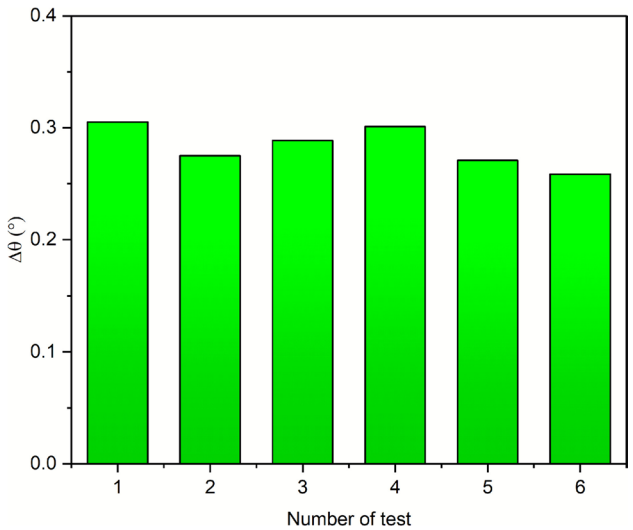

Figure 11 The reproducibility of Au/ZIF-8 sensor for the detection of Sb^{3+}.

the sensing layer. Furthermore, the *n* value obtained was 0.34 suggesting a high degree of heterogeneity relationships with antimony ions at the interface of the sensor surface [48].

To evaluate the reproducibility of the Au/ZIF-8 sensor, repeated SPR measurements were performed under the same experimental conditions. Figure 11 shows the overlay of SPR curves from six independent measurements, demonstrating excellent consistency in the resonance angle shifts, which confirms the stability and repeatability of the sensing layer. The relative standard deviation (RSD) calculated from six measurements was 5.86%, indicating that the designed sensor exhibits satisfactory reproducibility for Sb^{3+} detection.

Comparison of LOD values for detection of Sb^{3+} in comparison to other sensors

To further validate the analytical performance of the proposed SPR sensor, a comparative analysis of its detection capability was conducted against various established analytical techniques reported in the literature for Sb^{3+} determination. Table 2 summarizes the linear detection range and LOD achieved by different methods, including spectroscopic, chromatographic, electrochemical, and optical sensing approaches. This comparison provides a comprehensive benchmark to evaluate the sensitivity and practical applicability of the developed SPR-based sensing platform. As presented, a wide range of analytical techniques has been reported for the detection of Sb^{3+}, including fluorescence, atomic absorption spectrometry (AAS), chromatography coupled with plasma-based spectrometry, colorimetric methods, and UV–Vis spectroscopy. While some methods, such as fluorescence-based techniques, achieve sub-ppb LODs, they generally require

Table 2 Comparison of linear detection range and limit of detection (LOD) of different analytical methods for Sb^{3+} determination

Method	Range (ppm)	LOD (ppm)	References
Fluorescence	0.0015–91.32	0.00038	[50]
Fluorescence	0.001–0.030	0.0015	[51]
Flame AAS	–	0.31	[52]
Electrothermal AAS	–	0.45	[53]
Liquid chromatography with an inductively coupled plasma-optical emission spectrometry (LC-ICP-OES)	0–5	0.025	[54]
Colorimetry	0–1	0.0020	[55]
Colorimetry	0–25	0.6	[56]
UV–Vis spectroscopy	–	4.84	[57]
SPR	0.01–100	0.0589	This work

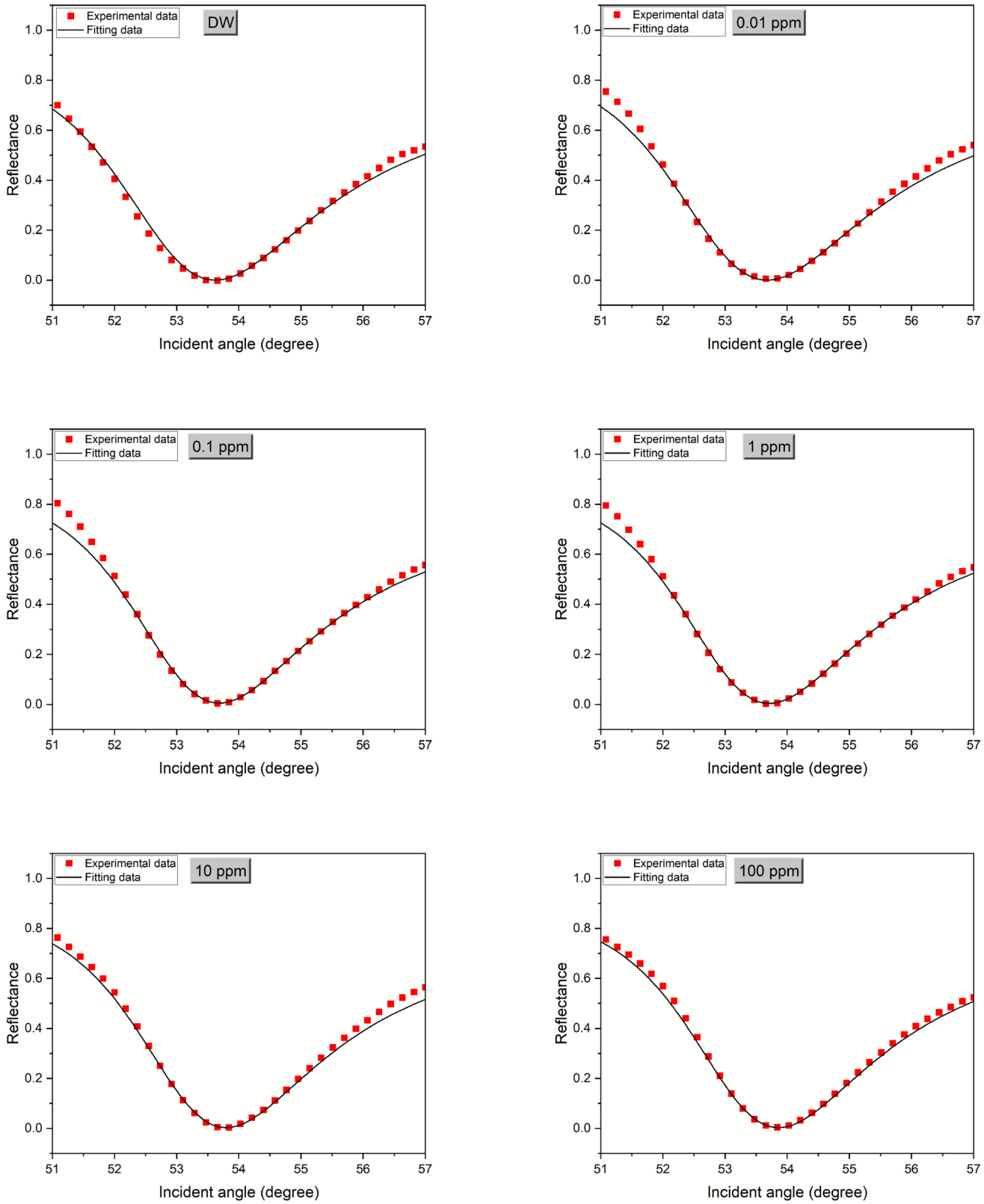

Figure 12 SPR experimental curve fitted to the theoretical data for Au/ZIF-8 thin film with different concentrations of Sb^{3+} (0–100 ppm).

Table 3 Refractive index of the Au/ZIF-8 after in contact with Sb^{3+} at different concentrations

Sb^{3+} concentrations (ppm)	Refractive index		Thickness, t (nm)
	Real part, (*n*)	Imaginary part, (*k*)	
0	1.3572	0.0040	9.59
0.01	1.3586	0.0040	9.59
0.1	1.3611	0.0040	10.39
1	1.3690	0.0040	10.44
10	1.3734	0.0033	12.39
100	1.3843	0.0033	14.39

complex procedures or specialized instrumentation. In contrast, the proposed SPR sensor offers a competitive detection limit along with a wide linear range, straightforward operation, and real-time sensing capability [49], underscoring its strong potential for practical applications in environmental monitoring.

Fitting of SPR curve to the theoretical data using transfer matrix method (TMM)

The experimental SPR reflectance curves were fitted using WinSpall software, in which the Fresnel equations were implemented through the transfer matrix method (TMM) to model the multilayer system [58]. This approach allowed accurate determination of the optical properties and thickness of the thin films. Figure 12 presents the experimental SPR curves of the Au/ZIF-8 sensor at different Sb^{3+} concentrations, along with the corresponding theoretical fits obtained from WinSpall. The experimental SPR curves closely follow the theoretical fits (black line), indicating that the fitting model accurately represents the optical behavior of the Au/ZIF-8 sensor. Aside from that, the fitting procedure allows for the determination of the refractive index and thickness of the sensing layer. From Table 3, at the initial concentration, the real part of the refractive index, *n*, and the imaginary part, *k*, were determined to be 1.3572 and 0.0040, respectively which are in close agreement with previous reported range of value [59]. At this concentration, we assume that no interactions occur, allowing the determination of the ZIF-8 sensor thickness, which was found to be 9.59 nm. Subsequent increases in the concentration of Sb^{3+} result in increases in both *n* and the thickness of the sensing layer, while the *k* value decreases, likely due to enhanced binding of the target ions to the sensing layer [60].

Conclusion

Overall, the FESEM, EDX, XRD, and BET characterisations confirm the successful formation and integration of ZIF-8 on the SPR sensing platform. FESEM revealed well-defined rhombic dodecahedral particles (262.60 ± 44.21 nm) with reduced agglomeration, while EDX verified the presence of C, N, Zn, and O consistent with ZIF-8. XRD patterns matched the JCPDS 00–062-1030 standard, and BET analysis indicated a predominantly microporous structure with a high surface area (991.81 m^2/g). For Sb^{3+} detection using SPR, the Au/ZIF-8 sensing layer demonstrated a clear and consistent rightward SPR shift with increasing concentration. The strong linearity ($R^2 = 0.95$), sensitivity of 0.057 ppm^{-1}, and binding affinity constant of 1.202 ppm^{-1} confirm the reliability and effectiveness of Au/ZIF-8 for antimony ion sensing within the tested range.

Acknowledgement

Open access funding provided by the Ministry of Higher Education Malaysia and Universiti Putra Malaysia. This research was funded by Universiti Putra Malaysia through Putra Grant (GPB/2024/9810900). The authors would like to acknowledge the laboratory facilities provided by the Institute of Nanoscience and Nanotechnology (ION2), Faculty of Engineering, and Faculty of Science (Department of Physics and Department of Chemistry), Universiti Putra Malaysia.

Funding

Open access funding provided by The Ministry of Higher Education Malaysia and Universiti Putra Malaysia.

Data availability

The data used in this study are available from the corresponding author upon reasonable request.

Declarations

Conflict of interest The authors declare that they have no conflict of interest.

References

[1] Abdelhamid HN (2021) Biointerface between zif-8 and biomolecules and their applications. Biointerface Res Appl Chem 11:8283–8297

[2] Tao C, Wang J, Chen R (2020) Metal organic frameworks-based optical thin films. Multilayer thin films-versatile applications for materials engineering. IntechOpen

[3] Paul A, Banga IK, Muthukumar S, Prasad S (2022) Engineering the ZIF-8 pore for electrochemical sensor applications-a mini review. ACS Omega 7:26993–27003

[4] Lin W, Rieter WJ, Taylor KML (2009) Modular synthesis of functional nanoscale coordination polymers. Angew Chem Int Ed Engl 48:650–658

[5] Salehifar N, Holtmann P, Hungund AP et al (2023) Calculations of adsorption-dependent refractive indices of metal-organic frameworks for gas sensing applications. Opt Express 31:7947. https://doi.org/10.1364/oe.478427

[6] Kim DW, Eum K, Kim H et al (2019) Continuous ZIF-8/reduced graphene oxide nanocoating for ultrafast oil/water separation. Chem Eng J 372:509–515. https://doi.org/10.1016/j.cej.2019.04.179

[7] Kumar P, Deep A, Kim KH (2015) Metal organic frameworks for sensing applications. TrAC Trends Anal Chem 73:39–53

[8] Vijayakumar E, Ramakrishnan S, Sathiskumar C et al (2022) MOF-derived CoP-nitrogen-doped carbon@NiFeP nanoflakes as an efficient and durable electrocatalyst with multiple catalytically active sites for OER, HER, ORR and rechargeable zinc-air batteries. Chem Eng J. https://doi.org/10.1016/j.cej.2021.131115

[9] Guan Y, Shi J, Xia M et al (2017) Monodispersed ZIF-8 particles with enhanced performance for CO_2 adsorption and heterogeneous catalysis. Appl Surf Sci 423:349–353. https://doi.org/10.1016/j.apsusc.2017.06.183

[10] Farrusseng D, Aguado S, Pinel C (2009) Metal-organic frameworks: opportunities for catalysis. Angew Chem Int Ed Engl 48:7502–7513

[11] Ding S, Yan Q, Jiang H et al (2016) Fabrication of Pd@ZIF-8 catalysts with different Pd spatial distributions and their catalytic properties. Chem Eng J 296:146–153. https://doi.org/10.1016/j.cej.2016.03.098

[12] Wang Q, Sun Y, Li S et al (2020) Synthesis and modification of ZIF-8 and its application in drug delivery and tumor therapy. RSC Adv 10:37600–37620

[13] Van TT, Dang HH, Nguyen H et al (2025) Synthesis methods, structure, and recent trends of ZIF-8-based materials in the biomedical field. Nanoscale Adv. https://doi.org/10.1039/d4na01015a

[14] Zhou W, Shen J, Lin J et al (2021) Zeolitic imidazolate framework nanoparticles loaded with gadolinium chelate as efficient T 1 MRI contrast agent. J Mater Sci 56:7386–7396. https://doi.org/10.1007/s10853-020-05647-7

[15] Lu H, Ke Z, Feng L, Liu B (2023) Voltammetric sensing of Cd(II) at ZIF-8/GO modified electrode: optimization and field measurements. Chemosphere. https://doi.org/10.1016/j.chemosphere.2023.138710

[16] Moscoso FG, Rodriguez-Albelo LM, Ruiz-Salvador AR et al (2023) Enhancement of the intrinsic fluorescence of ZIF-8 via post-synthetic cation exchange with Cd^{2+} and its incorporation into PDMS films for selective sulfide optical sensing. Mater Today Chem. https://doi.org/10.1016/j.mtchem.2022.101366

[17] Quang Khieu D, Thi Thanh M, Vinh Thien T et al (2018) Synthesis and Voltammetric Determination of Pb(II) Using a ZIF-8-Based Electrode. J Chem 2018:5395106

[18] Chu Y, Gao F, Gao F, Wang Q (2019) Enhanced stripping voltammetric response of Hg^{2+}, Cu^{2+}, Pb^{2+} and Cd^{2+} by ZIF-8 and its electrochemical analytical application. J Electroanal Chem 835:293–300. https://doi.org/10.1016/j.jelechem.2019.01.053

[19] Salandari-Jolge N, Ensafi AA, Rezaei B (2021) Ultra-sensitive electrochemical aptasensor based on zeolitic imidazolate framework-8 derived Ag/Au core-shell nanoparticles for mercury detection in water samples. Sens Actuators B Chem. https://doi.org/10.1016/j.snb.2020.129426

[20] Xu Y, Guo H, Wei Y et al (2024) Detection of heavy metal Pb^{2+} by electrochemical sensor based on ZIF-8@GO composite. J Appl Electrochem 54:1397–1407. https://doi.org/10.1007/s10800-023-02042-3

[21] Bech J, Corrales I, Tume P et al (2012) Accumulation of antimony and other potentially toxic elements in plants around a former antimony mine located in the Ribes Valley (Eastern Pyrenees). J Geochem Explor 113:100–105. https://doi.org/10.1016/j.gexplo.2011.06.006

[22] Filella M, Belzile N, Chen YW (2002) Antimony in the environment: a review focused on natural waters I. Occurence. Earth Sci Rev 57:125–176. https://doi.org/10.1016/S0012-8252(01)00070-8

[23] Bolan N, Kumar M, Singh E et al (2022) Antimony contamination and its risk management in complex environmental settings: a review. Environ Int. https://doi.org/10.1016/j.envint.2021.106908

[24] Cooper R, Harrison A (2009) The exposure to and health effects of antimony. Indian J Occup Environ Med 13:3. https://doi.org/10.4103/0019-5278.50716

[25] Li J, Wang Q, Oremland RS et al (2016) Microbial antimony biogeochemistry: enzymes, regulation, and related metabolic pathways. Appl Environ Microbiol 82:5482–5495

[26] Jayakumar N, Varghese J, Biju A et al (2024) Antimony and arsenic detection: review on electrochemical biosensors and their applications. Water Pract Technol 19:4062–4090. https://doi.org/10.2166/wpt.2024.246

[27] Anuar MF, Fen YW, Liew JYC et al (2025) Performance analysis of gold/graphene oxide surface plasmon resonance interface for trace level detection of cadmium ions. Eng Res Express 7:045005. https://doi.org/10.1088/2631-8695/ae04ca

[28] Topor CV, Puiu M, Bala C (2023) Strategies for surface design in surface plasmon resonance (SPR) sensing. Biosensors. https://doi.org/10.3390/bios13040465

[29] Gupta G, Kondoh J (2007) Tuning and sensitivity enhancement of surface plasmon resonance sensor. Sens Actuators B Chem 122:381–388. https://doi.org/10.1016/j.snb.2006.06.005

[30] Vinogradov AP, Dorofeenko AV, Pukhov AA, Lisyansky AA (2018) Exciting surface plasmon polaritons in the Kretschmann configuration by a light beam. Phys Rev B. https://doi.org/10.1103/PhysRevB.97.235407

[31] Cravillon J, Schröder CA, Bux H et al (2012) Formate modulated solvothermal synthesis of ZIF-8 investigated using time-resolved in situ X-ray diffraction and scanning electron microscopy. CrystEngComm 14:492–498. https://doi.org/10.1039/c1ce06002c

[32] Maya F, Palomino Cabello C, Clavijo S et al (2015) Zeolitic imidazolate framework dispersions for the fast and highly efficient extraction of organic micropollutants. RSC Adv 5:28203–28210. https://doi.org/10.1039/c5ra01079a

[33] Jafari N, Zeinali S (2020) Highly rapid and sensitive formaldehyde detection at room temperature using a zif-8/mwcnt nanocomposite. ACS Omega 5:4395–4402. https://doi.org/10.1021/acsomega.9b03124

[34] Ahmad K, Nde DT, Khan RA, Raza W (2024) Fabrication of Zeolitic imidazolate framework-8 (ZIF-8) modified screen-printed electrode and its catalytic role for the electrochemical determination of biological molecule (dopamine). Colloids Surf A Physicochem Eng Asp. https://doi.org/10.1016/j.colsurfa.2024.134606

[35] Kim E, Umar A, Ameen S et al (2023) Synthesis and characterizations of ZIF-8/GO and ZIF-8/rGO composites for highly sensitive detection of Cu2+ ions. Surf Inter. https://doi.org/10.1016/j.surfin.2023.103163

[36] Wu Y, Cao S, Xuan S et al (2020) High performance zeolitic imidazolate framework-8 (ZIF-8) based suspension: improving the shear thickening effect by controlling the morphological particle-particle interaction. Adv Powder Technol 31:70–77. https://doi.org/10.1016/j.apt.2019.10.001

[37] Tan PC, Ooi BS, Ahmad AL, Low SC (2017) Size control and stability study of zeolitic imidazolate framework-8 to prepare mixed matrix membrane. J Phy Sci 28:215–226. https://doi.org/10.21315/jps2017.28.s1.14

[38] Feng S, Jia X, Yang J et al (2020) One-pot synthesis of core–shell ZIF-8@ZnO porous nanospheres with improved ethanol gas sensing. J Mater Sci Mater Electron 31:22534–22545. https://doi.org/10.1007/s10854-020-04764-y

[39] Zhang Y, Jia Y, Hou L (2018) Synthesis of zeolitic imidazolate framework-8 on polyester fiber for PM2.5 removal. RSC Adv 8:31471–31477. https://doi.org/10.1039/c8ra06414h

[40] Malekmohammadi M, Fatemi S, Razavian M, Nouralishahi A (2019) A comparative study on ZIF-8 synthesis in aqueous and methanolic solutions: effect of temperature and ligand content. Solid State Sci 91:108–112. https://doi.org/10.1016/j.solidstatesciences.2019.03.022

[41] Lee TH, Oh JY, Hong SP et al (2019) ZIF-8 particle size effects on reverse osmosis performance of polyamide thin-film nanocomposite membranes: importance of particle

deposition. J Membr Sci 570–571:23–33. https://doi.org/10.1016/j.memsci.2018.10.015

[42] Lai LS, Yeong YF, Lau KK, Shariff AM (2016) Effect of synthesis parameters on the formation of ZIF-8 under microwave-assisted solvothermal. In: Proceedings Engineering. Elsevier Ltd, pp 35–42

[43] Seyed-Talebi SM, Kazeminezhad I, Motamedi H (2018) TiO2 hollow spheres as a novel antibiotic carrier for the direct delivery of gentamicin. Ceram Int 44:13457–13462. https://doi.org/10.1016/j.ceramint.2018.03.276

[44] Wu L, Li Y, Fu Z, Su BL (2020) Hierarchically structured porous materials: synthesis strategies and applications in energy storage. Natl Sci Rev 7:1667–1701

[45] Poupart R, Grande D, Carbonnier B, Le Droumaguet B (2019) Porous polymers and metallic nanoparticles: a hybrid wedding as a robust method toward efficient supported catalytic systems. Prog Polym Sci 96:21–42

[46] Hashim HS, Fen YW, Abdullah J et al (2025) Femtomolar detection of phenol using surface-modified plasmonic refractive index sensor with sodium carboxymethyl cellulose. Surf Interfaces. https://doi.org/10.1016/j.surfin.2025.107463

[47] Daniyal WMEMM, Bakar AAA, Bakar MHA et al (2025) Optimized potassium ion detection using angular interrogation SPR enhanced by multiwalled carbon nanotube-nanocrystalline cellulose. Photonic Sens. https://doi.org/10.1007/s13320-025-0758-0

[48] Molina-Calderón L, Basualto-Flores C, Paredes-García V, Venegas-Yazigi D (2022) Advances of magnetic nanohydrometallurgy using superparamagnetic nanomaterials as rare earth ions adsorbents: a grand opportunity for sustainable rare earth recovery. Sep Purif Technol. https://doi.org/10.1016/j.seppur.2022.121708

[49] Yanase Y, Hiragun T, Ishii K et al (2014) Surface plasmon resonance for cell-based clinical diagnosis. Sensors 14:4948–4959. https://doi.org/10.3390/s140304948

[50] Liu R, Wang Z, Hu X et al (2025) Smartphone-assisted fluorescence sensor based on AuNCs/ZIF-8 for highly selective detection of Sb^{3+} ions. Microchim Acta. https://doi.org/10.1007/s00604-025-06990-9

[51] Wei Q, Yang J, Zhang Y et al (2002) Determination of antimony(III) in environmental water samples in microemulsion system by the fluorescence quenching method. Talanta 58:419–426

[52] Ribeiro VS, Souza SO, Costa SSL et al (2020) Speciation analysis of inorganic As and Sb in urban dust using slurry sampling and detection by fast sequential hydride generation atomic absorption spectrometry. Environ Geochem Health 42:2179–2193. https://doi.org/10.1007/s10653-019-00488-z

[53] De Gregori I, Pinochet H, Fuentes E, Potin-Gautier M (2001) Determination of antimony in soils and vegetables by hydride generation atomic fluorescence spectrometry and electrothermal atomic absorption spectrometry. Optimization and comparison of both analytical techniques. J Anal At Spectrom 16:172–178. https://doi.org/10.1039/b008568p

[54] Moreno-Andrade I, Regidor-Alfageme E, Durazo A et al (2020) LC-ICP-OES method for antimony speciation analysis in liquid samples. J Environ Sci Health A Tox Hazard Subst Environ Eng 55:457–463. https://doi.org/10.1080/10934529.2019.1707565

[55] Berlina AN, Komova NS, Zherdev AV et al (2019) Colorimetric technique for antimony detection based on the use of gold nanoparticles conjugated with poly-A oligonucleotide. Appl Sci. https://doi.org/10.3390/app9224782

[56] Tighe M, Edwards MM, Cluley G et al (2018) Colorimetrically determining total antimony in contaminated waters and screening for antimony speciation. J Hydrol 563:84–91. https://doi.org/10.1016/j.jhydrol.2018.05.056

[57] González MJG, Renedo OD, Martínez MJA (2005) Simultaneous determination of antimony(III) and antimony(V) by UV-vis spectroscopy and partial least squares method (PLS). Talanta 68:67–71. https://doi.org/10.1016/j.talanta.2005.04.059

[58] Lu Y, Li M, Feng Y et al (2024) Tuning the optical properties of transparent ZIF-8 thin films by adjusting the crystal morphology. Opt Mater. https://doi.org/10.1016/j.optmat.2024.115714

[59] Omar NAS, Ramli I, Fen YW et al (2021) A sensing approach for manganese ion detection by carbon dots nanocomposite thin film-based surface plasmon resonance sensor. Optik. https://doi.org/10.1016/j.ijleo.2021.167435

[60.] Ji L, Chen Y, Yuan YJ (2014) Investigation of surface plasmon resonance phenomena by finite element analysis and Fresnel calculation. Sens Actuators B Chem 198:82–86. https://doi.org/10.1016/j.snb.2014.02.105